SUPPORTING INFORMATION

Fast and Sensitive Colloidal Quantum Dot Mid-Wave Infrared Photodetectors

Matthew M. Ackerman, Xin Tang, Philippe Guyot-Sionnest

James Franck Institute, 929 E. 57th Street, The University of Chicago, Chicago, IL 60637

List of supporting information:

1. Materials

Mercury (II) chloride (HgCl2, >99.5%, Sigma-Aldrich), Tellurium (pellets, 99.999%, Aldrich), Oleylamine (OAm, 70%, Aldrich), Trioctylphosphine (TOP, 97%, Aldrich), Silver nitrate (AgNO3, >99.0%, Sigma-Aldrich), Oleic acid (OA, 90%, Aldrich), 1,2-ethanediothiol (EdT, >98% Sigma-Aldrich), 1-dodecanethiol (DDT, >98%, Aldrich), Didodecyldimethylammonium bromide (DDAB, 98%, Sigma-Aldrich), Hydrochloric acid (HCl, 37% solution in water, Acros Organics), Chlorobenzene (BZC, 99.8%, Sigma-Aldrich), Octane (>99%, Sigma-Aldrich), Hexanes (HPLC grade, Fisher Chemical), Methanol (HPLC grade, Fisher Chemical), 2-propanol (isopropanol, Fisher Chemical), Acetone (Sigma-Aldrich), Butyl acetate (>99.5%, Sigma-Aldrich).

2. Instrumentation

Infrared spectra were taken using a Nicolet Magna-IR 550 spectrometer on a thin film supported by a ZnSe substrate. An Agilent Cary 5000 UV-Vis-NIR spectrometer was used to record spectra between 500 nm and 1800 nm. A home-built step-scan Michelson interferometer using an 808 nm source and MCT detector was used to measure the infrared photoluminescence. Transmittance electron microscopy (TEM) images were taken using a Tecnai Spirit with a driving voltage of 120 kV. X-ray photoelectron spectroscopy (XPS) results were obtained using a Kratos Axis Nova XPS system. Metal electrodes were deposited using an AJA ATC-Orion 8E e-beam evaporator operated at 10^{-8} torr. Sputter deposition was performed using an AJA Orion 5 UHV sputtering system at a pressure of 10^{-7} torr. A Femto DLPCA-200 variable gain low-noise transimpedance amplifier in series with a Stanford Research SR560 low-noise preamplifier was used to measure the photocurrent of a device. Noise spectrum analysis was performed using a

Stanford Research SR760 FFT Spectrum Analyzer. National Instruments DAQ and Labview software were used to record current-voltage and temperature-current data. An Agilent 33220A Waveform Generator was used to perform current-voltage and capacitance-voltage measurements.

3. Spectral characterization of Ag_2Te

Vis-NIR spectroscopy taken on a Cary 5000 UV-Vis-NIR spectrometer was used to characterize the Ag_2Te nanoparticles. The lack of an optical feature at ~1200 nm was used as an indicator that the Ag_2Te nanoparticles would yield good devices, while batches of the smaller Ag_2Te that had an optical feature were not beneficial to device performance.

A cation exchange with a methanolic solution of $HgCl_2$ with Ag_2Te in tetrachloroethylene was performed and Fourier transform infrared spectroscopy (FTIR) was taken of the resulting nanoparticles. After cation exchange, the formation of HgTe was verified by a broad absorption edge at ~4000 cm^{-1}. The absorption at ~2900 cm^{-1} was due to the surface ligands such as 1-dodecanethiol present before and after $HgCl_2$ treatment. The photoluminescence of the nanoparticles after cation exchange also strongly supports a high degree of conversion, as indicated by the change in photoluminescence intensity before and after exchange. The photoluminescence is an indication of the presence of HgTe following the exchange, as Ag_2Te does not emit in the infrared.

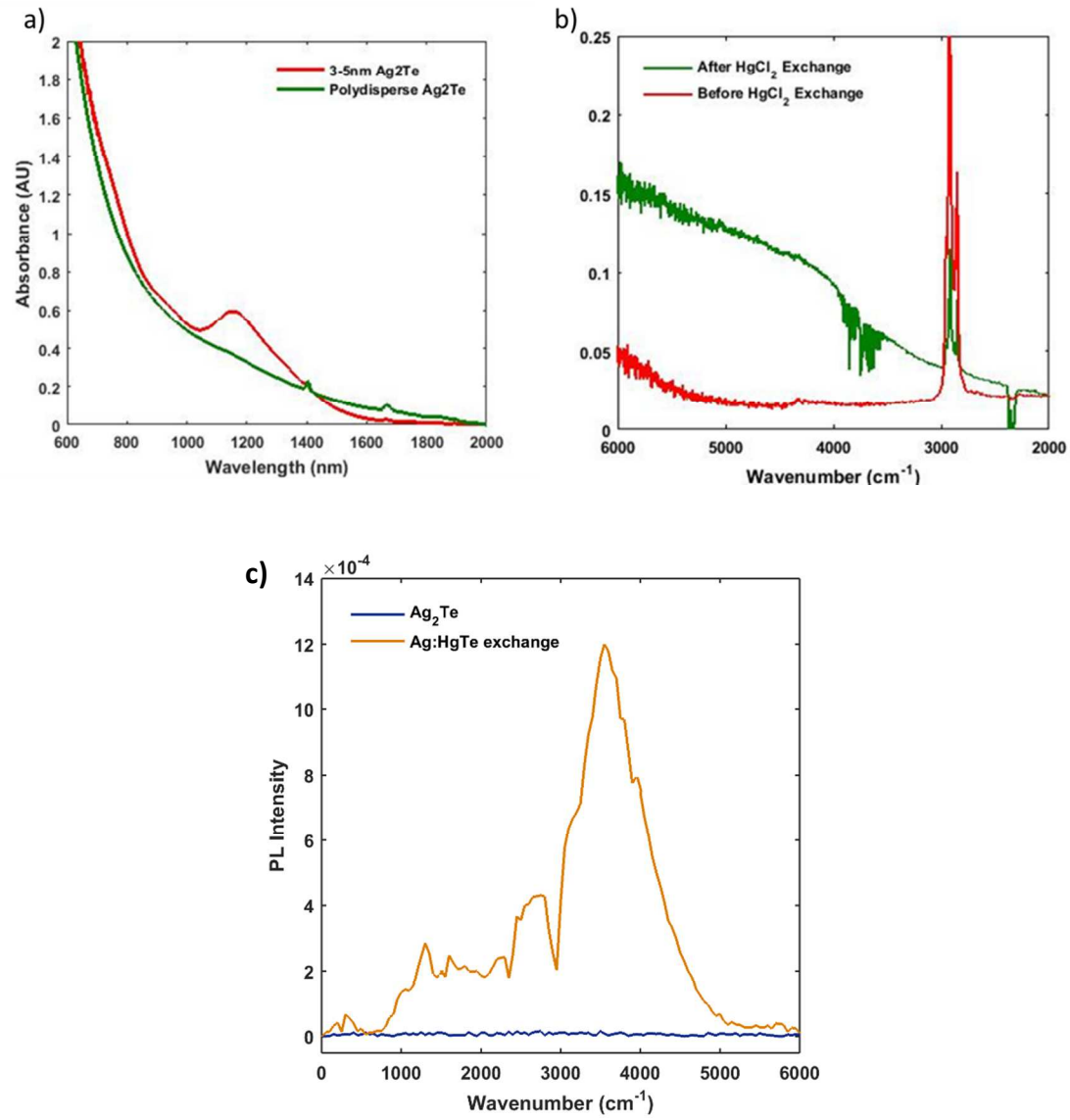

Fig.S1 (a) Vis-NIR spectra of Ag_2Te for two reactions. Small nanoparticles were produced by performing the reaction, reported in the Methods section, at 120 ^{o}C and is shown (red) in comparison with an ideal batch of Ag_2Te nanoparticles (green). (b) FTIR spectra of Ag_2Te nanoparticles before (red) and after (green) cation exchange in solution with $HgCl_2$. (c) Photoluminescence intensity of Ag_2Te nanoparticles before (blue) and after (yellow) phase exchange in solution. The photoluminescence is typical of HgTe CQDs with sizes between 5 – 10 nm.

4. Transmission electron microscopy images of Ag_2Te nanoparticles

Transmission electron microscopy (TEM) with a driving voltage of 120 keV was used to capture shape and size of the Ag_2Te nanoparticles. Two size distributions, each for different Ag_2Te syntheses, are provided for comparison between a desirable and undesirable batch of nanoparticles. A reliable, working device uses Ag_2Te that have a broader size distribution with larger nanoparticles, as previously indicated in spectral characterization.

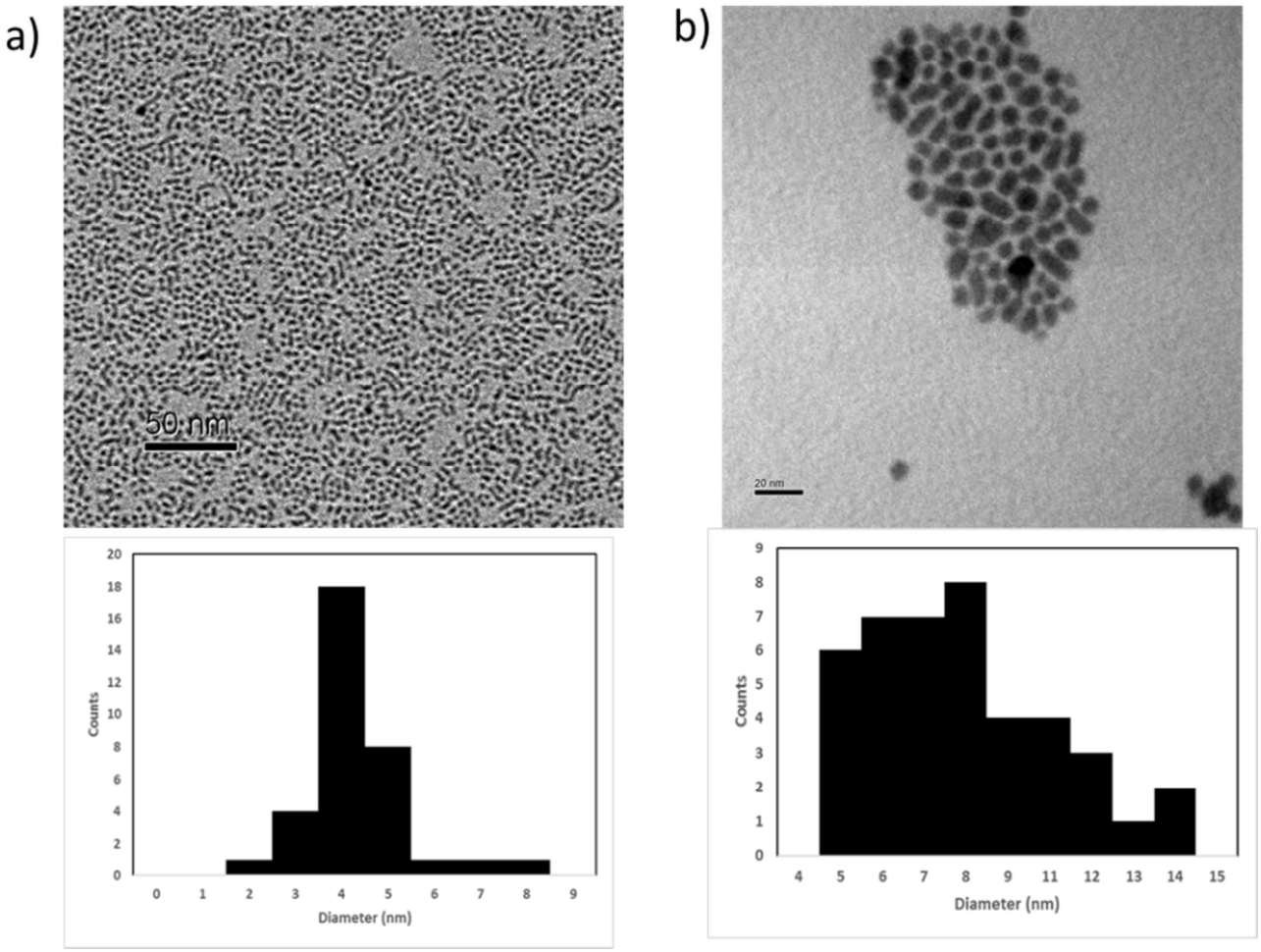

Fig.S2. (a) Small Ag_2Te nanoparticles with size distribution 4±1 nm. Scale bar is 50 nm. Vis-NIR of nanoparticles reveals optical feature at ~ 1200nm, as seen in Fig.S1a. (b) Larger,

polydisperse Ag_2Te with sizes between 5 nm and 14nm diameter. Scale bar is 20 nm. The corresponding Vis-NIR has no significant optical feature at ~1200 nm.

5. X-ray photoelectron spectroscopy of Ag_2Te and $HgCl_2$-treated Ag_2Te

X-ray photoelectron spectroscopy (XPS) was used to determine the chemical composition of Ag_2Te thin films before and after treatment with $HgCl_2$ methanol solution. A silicon piece was used as substrate. High resolution XPS spectra follow and the shift in the peak positions for tellurium, silver, and mercury were used to change in chemical composition. A shift of the tellurium peak, seen in Fig. S3a, from 572.3 eV before treatment to 572.9 eV after $HgCl_2$ treatment indicates a change in the tellurium environment due to interaction with Hg instead of Ag. The small shoulder at 576.5 eV indicates tellurium oxidation after solid-state exchange. Negative shifts in the Ag3d peaks at 368.1 eV and 374.1 eV to 367.6 eV and 373.6 eV, respectively, after exposure to $HgCl_2$ are attributed to the presence of AgCl species. The strong increase in the presence of Hg, indicated by the new peaks at 100.6 and 104.6 eV after exposure, are expected. However, $HgCl_2$ typically has a binding energy at approximately 101.4 eV; therefore, we attribute the shifted peak positions for Hg species to energies for HgTe. A full spectral comparison provides an atomic ratio of 39:41:9:12, which is approximately 4:4:1:1, for Ag: Cl: Hg: Te. It is inferred from the increased presence of Ag and Cl that a AgCl species exists on the surface of the nanoparticles, while the bulk composition is that of HgTe.

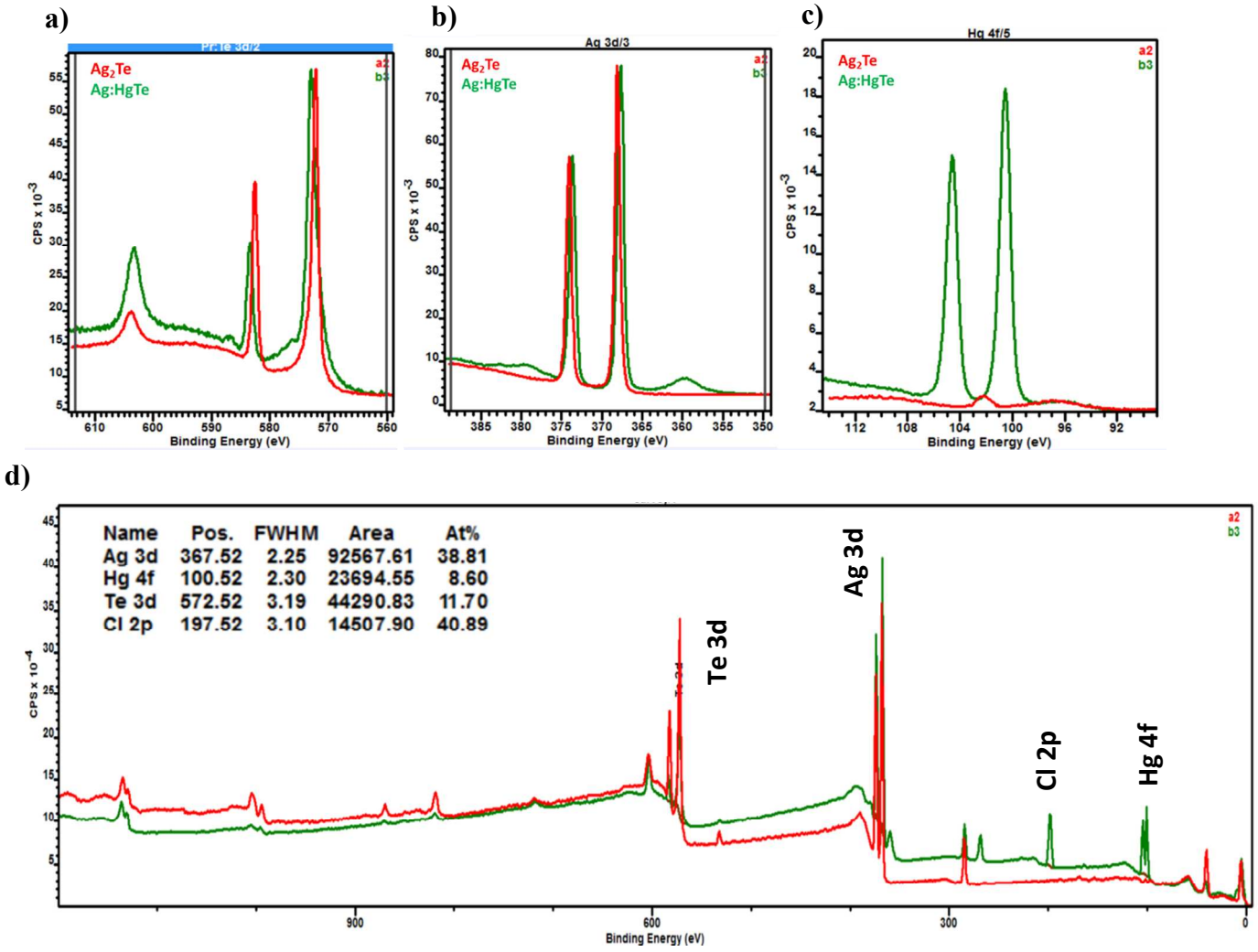

Fig.S3 XPS spectra for Ag_2Te before (red) and after (green) treatment by $HgCl_2$. (a) Te3d peak at 572.3 eV before treatment shifts to 572.9 eV after $HgCl_2$ treatment, with a small peak at 576.5 eV indicating tellurium oxidation. (b) Ag3d peak at 368.1 eV and 374.1 eV before $HgCl_2$-treated shift to 367.6 eV and 373.6 eV, respectively, after exposure. (c) Hg4f peaks at 100.6 eV and 104.6 eV are shown after the $HgCl_2$ treatment. (d) Full XPS spectrum used to determine atomic

ratios. Peaks are labelled to indicate use in analysis and the inset table provides high resolution atomic percentages.

6. Secondary ion mass spectrometry

Secondary ion mass spectrometry (SIMS) was performed by Nanolab Technologies Inc. on two samples with and without the $HgCl_2$ treatment. Data are shown in Fig.S4. The concentration of each element is normalized with respect to a value of Indium 5×10^{22} cm^{-3} taken for the ITO thin films. The element concentrations are not justified since the Hg concentration would for example be higher than bulk HgTe ($1.49x10^{22}$ cm^{-3}). This is due to the uncalibrated relative sensitivity of the instrumentation to different ions.

Only relative changes as a function of depth are meaningful. For example, the content of Ag in the first 30 nm for the $HgCl_2$ treated device (sample I) is about 3-fold lower than without $HgCl_2$.

The SIMS data failed to provide detailed depth information on the Ag content. Although SIMS would be sensitive enough to detect small Ag concentrations, the beam kicks the Ag atoms into the film because of the film porosity. This even shows up as an accumulation next to the compact ITO layer. Therefore, for such materials, a different SIMS measurement would need to be carried out to characterize the Ag concentration, likely from starting from the ITO side. Such custom measurements will be of interest in future investigations of the doping profile.

Most obvious from SIMS is the difference in chloride content between samples. The HgCl2 treatment leads to 10-fold increase in Cl concentration. Free chloride ions are soluble in IPA and unlikely to remain in the film after washing the device. However, surface bound chloride as $HgCl_2$ species may remain. Treatment with metal halides on PbS and PbSe CQDs increased

power conversion efficiencies by improving both short-circuit current and open-circuit voltage. [Scientific Reports volume 5, Article number: 9945 (2015); J. Phys. Chem. Lett., 2015, 6 (15), pp 2892–2899]. The use of $HgCl_2$ directly on a film of HgTe, without the Ag2Te CQD layer quenched the device performance. Therefore, the use of an Ag_2Te film may reduce the reactivity of $HgCl_2$ in addition to acting as a dopant for HgTe following cation exchange.

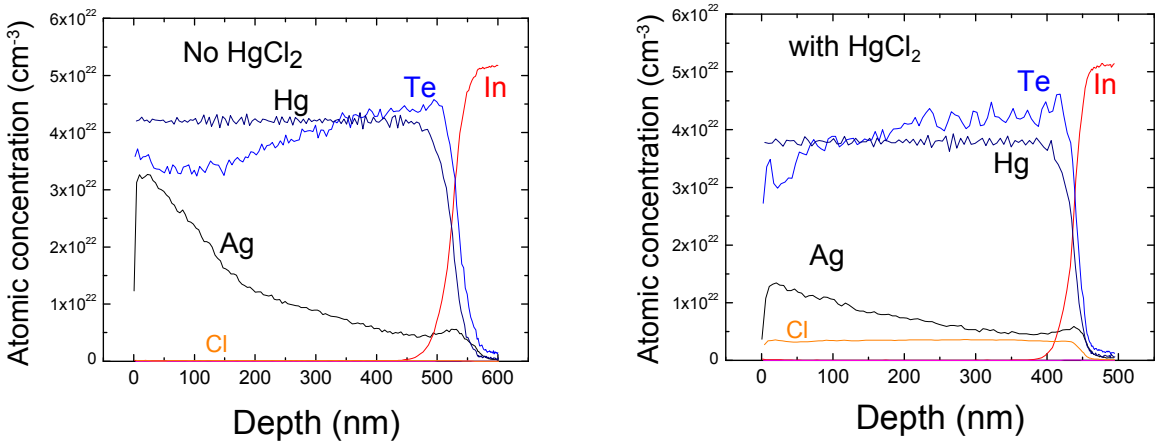

Fig.S4: SIMS data for a sample without the HgCl2 treatment (left) and with the HgCl2 treatment (right). Data from Nanolab Technologies, Inc. Sulfur concentration was ~ $10^{19}cm^{-3}$ on that scale.

7. Optimization of thickness of Ag2Te CQDs layer

The thickness of Ag_2Te CQDs layer can be optimized. Three groups of HgTe CQDs photodetectors were fabricated by using Ag_2Te CQDs solution in 9:1 hexane:octane with different concentrations of 12.5 mg/ml, 6.25 mg/ml, and 3.125 mg/ml. The Ag2Te CQDs solutions were spin-coated at room temperature. The resulted responsivity at 85 K were 0.42 A/W, 0.74 A/W, and 0.27 A/W, respectively, as shown in Fig.S4. Therefore, 6.25 mg/mL solution would give the optimum thickness of Ag_2Te CQDs film on the detector. Besides

thickness of Ag_2Te CQDs film, we also explored the influence of $HgCl_2$ treatment time on the device performance. For the optimum thickness of Ag_2Te CQDs film, we found 10 sec is a suitable treatment time. The sample treated with $HgCl_2$ for less than 5 s showed significantly decreased photocurrent at room temperature and non-rectifying IV curve at 85 K. Longer treatment times (> 30 s) lead to increased device resistance, which degraded the photoresponse.

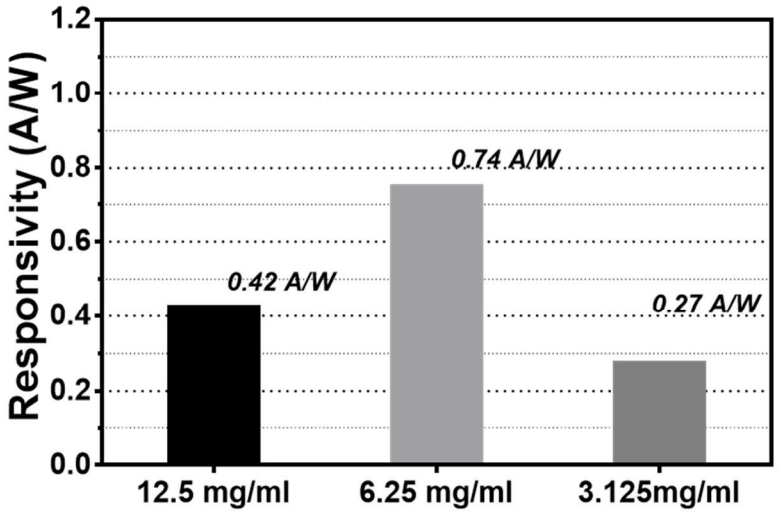

Fig.S5 The responsivity of HgTe CQDs MWIR detector fabricated by using Ag_2Te CQDs solution with three different concentrations.

8. Carrier concentration per dot calculation

From TEM, the HgTe CQDs are tetrahedra. Taking the volume of a tetrahedron to be

$$V = \frac{a^3}{6 * \sqrt{2}}$$

and the edge length of the CQDs a = 11 ± 1 nm, the volume per dot is $1.6 \pm 0.4 \times 10^{19}$ cm^3/dot.

To determine the concentration of carriers per dot, N_{NC}, when given carriers per cm^3, N,

$$N_{NC} = N * \frac{V_{QD}}{F}$$

where V_{QD} is the quantum dot volume, F is the packing fraction of the CQD thin film taken to be 0.6 ± 0.1.

Similarly, when determining the concentration per cm^3 from the concentration per dot, the previous expression is rearranged. In both cases, the standard error propagation formula is used to determine the error in the concentration.

9. Estimation of internal quantum efficiency

The internal quantum efficiency (*IQE*) is defined as:

$$IQE = \frac{I_{ph}/e}{\varphi_{abs}} \quad (1)$$

where I_{ph} is the photocurrent, e is the elementary charge, and φ_{abs} is the absorbed photon flux by the HgTe CQDs film, which can be calculated by integrating the product of spectral absorbance $abs(\omega)$ and incident photon flux $\varphi(\omega)$:

$$\varphi_{abs} = \int abs(\omega) \cdot \varphi(\omega) d\omega = \int abs(\omega) \cdot (2hc^2 \frac{\omega^3}{e^{\frac{hc\omega}{k_B T}} - 1} \cdot A \cdot \Omega \cdot t) d\omega \quad (2)$$

where h is the Planck's constant, c is the speed of light, ω is the wavenumber, k_B is the Boltzman's constant, T is the blackbody temperature, A is the sensing area, Ω is the solid angle, and t is the optical transmission of the CaF_2 cryostat window.[1] The spectral optical absorption $abs(\omega)$ of HgTe CQDs film is simulated by using COMSOL Multiphysics. Fig.S5a illustrated the

device model in the simulation. The thickness and index of refraction of the HgTe CQDs is set to be 400 nm and 2.3+0.1i, respectively. The simulated spectral absorbance and incident photon flux are shown in Fig.S5b. Based on Eq1 and Eq2, the *IQE* of the HgTe CQDs with responsivity of 0.74 A/W is estimated to be ~95.7%.

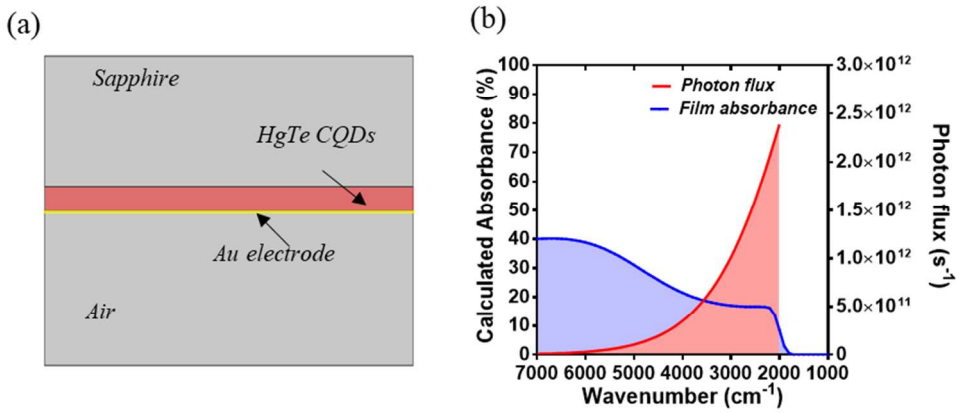

Fig.S6 (a) Device model of HgTe CQDs without interference structure. (b) Plot of calculated absorbance and photon flux as a function of wavenumber.

10. The single-pixel scanning camera

The single pixel scanning camera mainly consist of six parts: ZnSe lens, motorized XY linear stages, HgTe CQDs MWIR detector, amplifier, DAQ, and up-level software. The ZnSe lens with a 30mm focal length is mounted on the motorized XY stage. The maximum scanning range is 25 mm × 25 mm. While scanning, the photocurrent is amplified, digitalized, and recorded, based on which the thermal image is constructed.

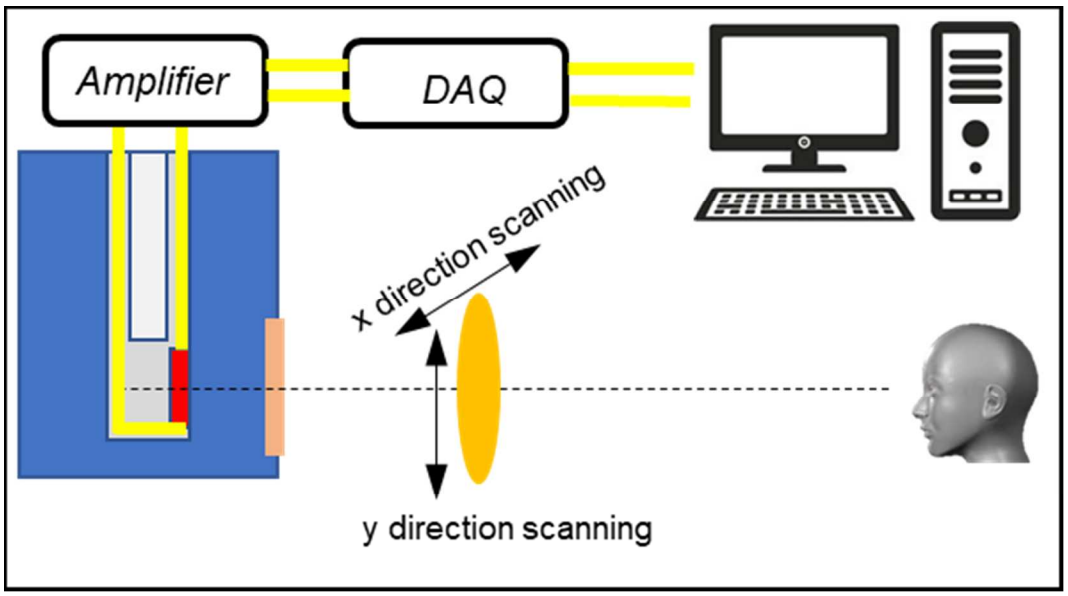

Fig.S7 The setup of the single pixel camera system.

11. Transmission electron microscopy image and spectra of HgTe quantum dots

Transmission electron microscopy (TEM) images of HgTe CQDs were captured under a 120 kV electron beam driving voltage. The nanoparticles are ~ 8-9 nm along the longest edge when measured under TEM. The HgTe CQDs aggregate in solution. As a consequence of the aggregation, a size distribution was not available by direct imaging. Therefore, the photoluminescence linewidth and sharpness of the absorption edge are used to quantitatively assess the quality of the nanoparticle solution. The photoluminescence linewidth of 650 cm^{-1} at 300 K was typical of HgTe CQDs, following the reported synthesis. Additionally, the absorption spectrum has a sharp cutoff with a 90%-to-10% width of 580 cm^{-1} and half-width at half-maximum of 560 cm^{-1} taking the maximum as the onset of the shoulder at 3220 cm^{-1}. As an example, for this spectrum at room temperature, the cutoff wavelength defined as the half-point of the absorption shoulder is at 3.8 μm (2650 cm^{-1}).

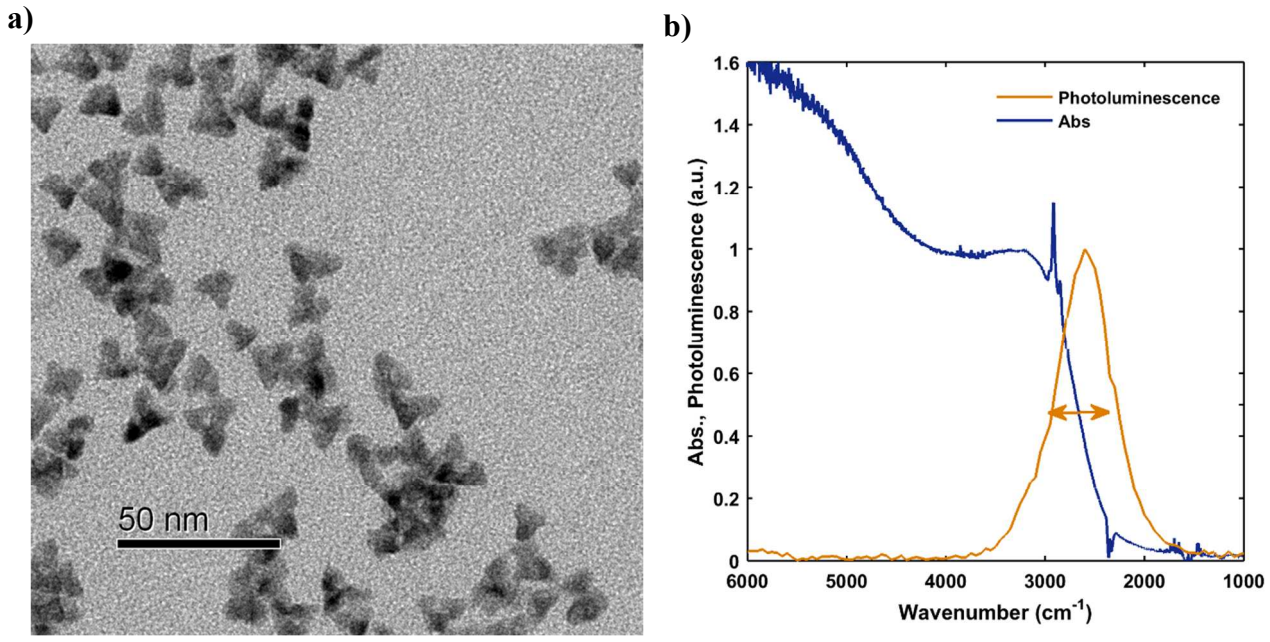

Fig S8. Transmission electron microscopy and spectral characteristics for HgTe CQDs. (a) TEM image of HgTe CQDs, which show partial aggregation. (b) Absorption (blue) and photoluminescence (yellow) for HgTe CQDs.

12. Thin film uniformity

To demonstrate the film quality of the HgTe thin films prepared by dropcasting, the following image is presented. In the image, the inverted characters are made visible by the smooth, highly reflective film of HgTe CQDs prepared for a device. On the sample are six gold contacts, each one a device with area ~ 1 mm^2 where the contact overlaps with the underlying ITO in the center of the substrate. An SEM image and AFM line profile of a Ag_2Te/HgTe thin film stack are also shown to demonstrate the film uniformity after treatment with $HgCl_2$. From the SEM image, it can be seen the film appears highly uniform with minimal defects over a 30 x 30 μm^2 area. The AFM line profile over a 7 μm scan has an average surface roughness of 10 nm, approximately the length of one CQD.

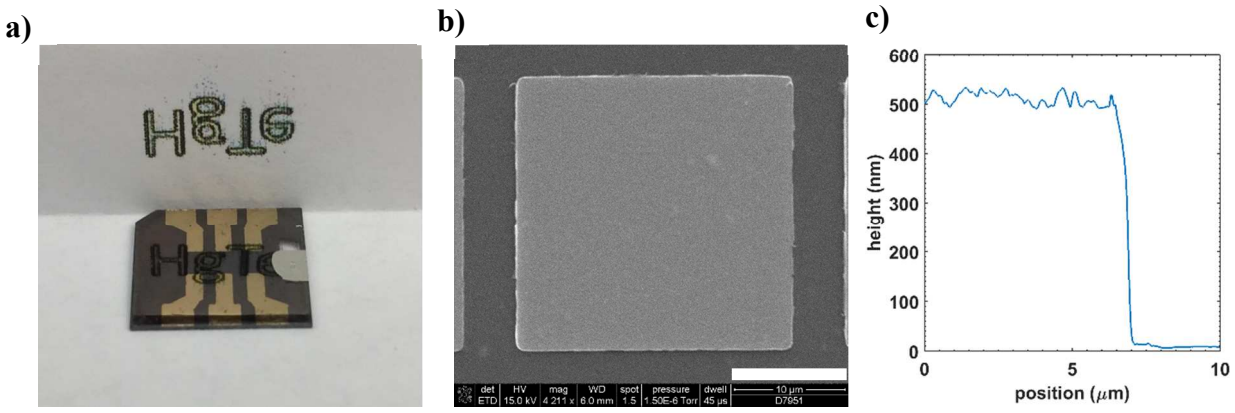

Fig. S9. Ag_2Te/HgTe thin film prepared on ITO/sapphire substrate. (a) The inverted characters are reflected by the film of CQDs, demonstrating the smooth quality of dropcast films. (b) An ~ 30 x 30 μm^2 pixel of Ag_2Te/HgTe CQDs with high uniformity after $HgCl_2$ exposure. White scale bar is 10 μm. (c) Line scan profile from AFM measurement with an average surface roughness of 10 nm after $HgCl_2$ treatment.

References:

1. Kramm, G. & Mölders, N. Planck's Blackbody Radiation Law: Presentation in Different Domains and Determination of the Related Dimensional Constants. (2009).